Key Engineering Materials
ISSN: 1662-9795, Vol. 926, pp 2092-2098
doi:10.4028/p-kr1716
© 2022 The Author(s). Published by Trans Tech Publications Ltd, Switzerland.
Submitted: 2021-12-14
Revised: 2022-01-20
Accepted: 2022-01-23
Online: 2022-07-22

Fracture Characterization of Advanced High Strength Steel USS CR980XG3 Using Phase-Field Diffusive Approach in Ductile Solids

Erfan Azinpour[1,a], Manuel Jimenez[2,b], Abel D. Santos[1,2,c*] and Jose Cesar de Sa[1,2,d]

[1*]Department of Mechanical Engineering, Faculty of Engineering, University of Porto, Portugal

[2]Institute of Science and Innovation in Mechanical and Industrial Engineering, Porto, Portugal

[a]azinpour@fe.up.pt, [b]mabarca@inegi.up.pt, [c]abel@fe.up.pt, [d]cesarsa@fe.up.pt

Keywords: Advanced steels, Crack analysis, Phase-field model.

Abstract. In this work, the utilization of a phase-field ductile fracture model in the failure analysis of advanced steels is investigated. The importance of advanced steels is potentially proven, for instance in automotive industry, due to its light weight, which entails the crucial role of fracture analysis in these structures. A third generation advanced high strength USS CR980XG3™ AHSS material is considered to perform fracture analyses. For this purpose, the necessary data regarding the stress distribution and fracture patterns from digital image correlation tests are utilized for subsequent numerical experimentations.

A recent phase-field model of ductile fracture is employed herein for the analysis of crack advance in this class of materials. The significance of the choice of material properties using this model is shown through the analysis of an experimental fracture benchmark called Shear Fracture specimen, through assessment of crack evolution and force diagrams.

1. Introduction

Demands for lower emissions have prompted the development of a third generation of advanced high strength steels with a better strength/ductility balance, allowing structures to be lighter [1]. The use of numerical tools such as Finite Element (FE) methods is pivotal to predict the fracture behavior of these novel materials during the metal forming process. The recently developed phase-field models of fracture, classified under the variational approaches in fracture, shed valuable insights into the physics of crack advance in solids and it has become a significant competitive numerical tool in the analysis of fracture since its inception. The use of the phase-field diffusive fracture models, initially popularized in the brittle fracture setting [2], gained an enormous interest among researchers due to its straightforward implementation in FE framework and ability to analyze complex crack patterns, such as crack merging and bifurcation, in multi-dimensional settings and without the need for any ad hoc criteria as opposed to conventional fracture mechanics methodologies. Among many other applications, to date, this methodology is utilized and investigated in ductile materials framework in Miehe et al. [3], Ambati et al. [4], Borden et al. [5] and Samaniego et al. [6], just to name a few.

In this contribution, particularly focused on third generation AHSS, several experimental tests were designed to determine the forming limits and work hardening behavior of this class of material [7]. As for the numerical analysis of fracture, a recently developed phase-field approach in ductile fracture [8] is employed. A parameter represents the plastic work threshold level is considered here that could serve to regulate the interplay between the plastic dissipation and elastic energy contribution, which could have a significant influence on the material plastic hardening and post-critical softening regimes. As for the experimental validation, the simulated material response is evaluated against the laboratory data in terms of the force diagrams. Furthermore, qualitative assessment of crack advance is investigated. By drawing relevant comparisons with the experimental measurements, satisfactory results were achieved.

This article is an open access article under the terms and conditions of the Creative Commons Attribution (CC BY) license (https://creativecommons.org/licenses/by/4.0)

2. Material Characterization and Experimental Procedure

Table 1 summarizes the mechanical properties of USS CR980XG3™ AHSS in the sheet rolling direction including elastic properties, Young's modulus (E) and Poisson ratio (ν), as well as yield strength (R_p), ultimate tensile strength (R_m), uniform elongation (e_u) and total elongation (e_t) determined by uniaxial tensile test in specimens of 1.58 mm thickness [7].

Table 1: Mechanical properties of USS CR980XG3™ AHSS [7].

E [MPa]	ν [-]	R_p [MPa]	R_m [MPa]	e_u [%]	e_t [%]
192000	0.289	604	1040	18.0	23.4

Table 2 shows the modified Swift law's parameters for modeling the hardening curve and the anisotropy ratios represented by Lankford coefficients for 0°, 90°, and 45° relative to the rolling direction [7].

Table 2: Anisotropic Lankford coefficients and hardening parameters of USS CR980XG3™ AHSS [7].

R-value			Modified Swift law (RD – Rolling Direction)				
0°	45°	90°	K[MPa]	ε_0	n	m	$\dot{\varepsilon}_0[s^{-1}]$
0.861	0.957	0.895	1880	0.0069	0.231	0.0098	$^{2.6} \times 10^{-3}$

Electrical discharge machining was used to generate the Shear Fracture specimen from a 1.58 mm thickness of material sheet. Figure 1 illustrates the geometry dimensions of the Shear Fracture specimen. An in-plane shear geometry sample manufactured from dual-phase 980 AHSS steel based on Lou et al. [10] is adopted in this work for experimental and numerical study. The information regarding the notches can be found in the original publication in [10]. In this study, the length of the specimen is considered as 99 mm and the specimen has its longitudinal dimension along sheet rolling direction.

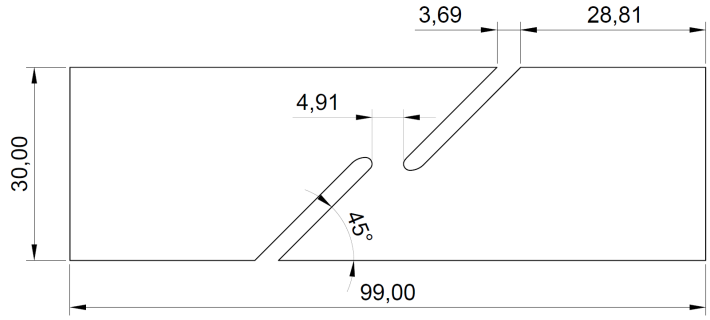

Figure 1: Dimensions in mm of Shear Fracture specimen.

All specimens were tested at a constant crosshead speed of 0.3 mm/min corresponding to a strain rate of 1×10^{-3}/s. The tests were carried out on an INSTRON 5900R testing equipment with a 100 kN load cell at room temperature. Figure 2a shows the set-up of the experiment. The images are taken at a frequency of 6 Hz using a 5 MPixel camera (Basler acA2440-75um, 2448x2048 pixels) with a high resolution lens (Fujinon HF50HB-1B, f2.3/50 mm). To determine the strain field using Digital Image Correlation (DIC), the specimens were painted prior to testing with a high-contrast stochastic speckle pattern of 50 µm size across the area of interest as shown in Fig. 2b.

The displacement field of the specimens was obtained using the DIC technique and the software VIC2D-Correlated solutions. The correlation analysis employs a subset size of 31 pixels and a step size of 7.

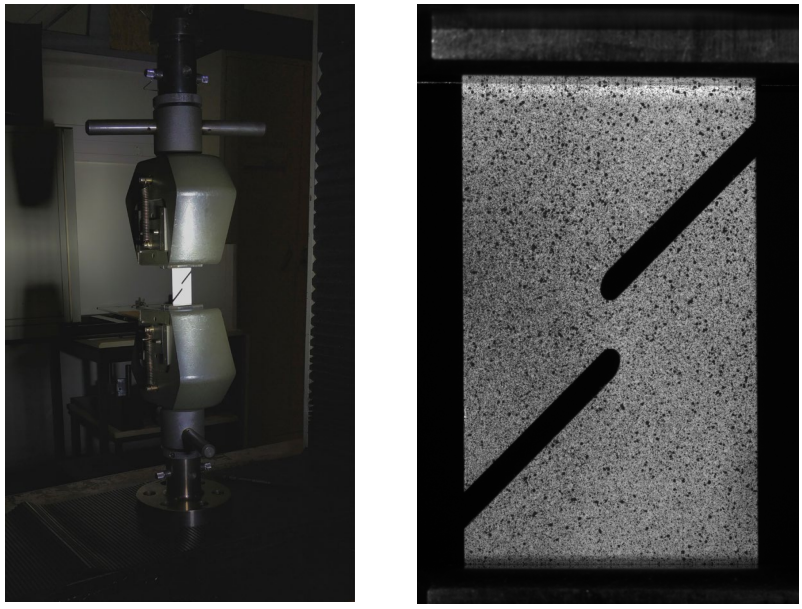

(a) (b)

Figure 2: (a) Specimen set-up on tensile test machine and (b) speckle pattern for displacement extraction using DIC.

3. Phase-Field Approach in Ductile Fracture

The inelastic fracture behavior of the material is analyzed using a phase-field approach in ductile fracture. Following regularization of the energy density based on the Griffith theory of brittle fracture, Miehe et al. [9] developed a phase-field framework based on thermodynamical considerations that could be readily implemented into the FE framework. Following the formulation in [8], we assume a solid with domain $\Omega \subset \mathbb{R}^n, n \in [1,2,3]$ with external boundary $\partial\Omega \subset \mathbb{R}^{n-1}$ and Γ as the crack interface. Throughout this work, we restrict our attention to the isothermal and small strain conditions where the total strain can be written based on the prescribed displacement field $\boldsymbol{u}$ as:

$$\boldsymbol{\varepsilon} = (\nabla \boldsymbol{u} + \nabla \boldsymbol{u}^T)/2 \tag{1}$$

The crack diffusion using phase-field method is carried out by assuming a phase-field order parameter, $d \in [0,1]$, distinguishes between the undamaged ($d = 0$) and fully-damaged ($d = 1$) material states. In the variational format, the total potential energy of an elastoplastic solid can be stated as a competition between the elastic, plastic and surface energy densities, given by:

$$\Pi(\boldsymbol{u}, d) = \Pi^e(\boldsymbol{u}, d) + \Pi^p(\alpha, d) + \Pi^s(d) \tag{2}$$

with α as the accumulated plastic strain to be defined. The elastic energy density over the volume of the solid, V, is written as:

$$\Pi^e(\boldsymbol{\varepsilon}, d) = \int_\Omega \psi^e(\varepsilon, d)\,\mathrm{dV} = \int_\Omega g(d)\psi_0(\boldsymbol{\varepsilon})\,\mathrm{dV} \tag{3}$$

with ψ_0 as the reference elastic energy density given by:

$$\psi_0(\varepsilon) = \frac{1}{2}\boldsymbol{\varepsilon}^{eT}\mathbf{D}^e\boldsymbol{\varepsilon}^e. \tag{4}$$

In the above equation, $\boldsymbol{\varepsilon}^e = \boldsymbol{\varepsilon} - \boldsymbol{\varepsilon}^p$ is the elastic strain tensor, with $\boldsymbol{\varepsilon}$ and $\boldsymbol{\varepsilon}^p$ as total strain and plastic strain tensors, respectively, and $\mathbf{D}^e$ is the linear elastic stiffness matrix. Notice that the above stored energy is affected by a phase-field degradation function, $g(d)$. The choice of this function

requires to ensure the properties $g(0) = 1$, $g(1) = 0$, $g'(1) = 0$. In this work, common choice of a quadratic degradation function is used:

$$g = (1 - d)^2. \tag{5}$$

The plastic contribution in Eq. 3 consists of the effective plastic work density function and plastic dissipation as follows:

$$\Pi^p(\alpha, d) = \int_\Omega g_d \left(\frac{1}{2} H\alpha^2 + \sigma_y \alpha\right) \mathrm{dV} \tag{6}$$

with H being the hardening modulus and σ_y is the material yield limit. Following the J2-plasticity and linear isotropic hardening law, the region of the purely elastic material response is identified for $\varphi < 0$, with φ being the material yield function, defined as:

$$\varphi(\boldsymbol{u}, H_\alpha) = \tilde{\sigma}(\boldsymbol{u}, \alpha) - H_\alpha = \tilde{\sigma}(\boldsymbol{u}, \alpha) - (\sigma_y + H\alpha) \tag{7}$$

where $\tilde{\sigma}$ is the equivalent von Mises stress. According to an associated plastic flow rule, the evolution laws for the internal variables can be obtained as:

$$\dot{\boldsymbol{\varepsilon}}^p = \dot{\gamma} \frac{\partial \varphi}{\partial \boldsymbol{\sigma}} \tag{8}$$

$$\dot{\alpha} = \dot{\gamma} \frac{\partial \varphi}{\partial H_\alpha} \tag{9}$$

where $\dot{\gamma}$ is the plastic multiplier and $\frac{\partial \varphi}{\partial \boldsymbol{\sigma}}$ is the plastic flow direction, i.e., the normal to the yield surface. The plastic multiplier is restricted by the following Kuhn-Tucker conditions:

$$\dot{\gamma} \geq 0, \quad \varphi \leq 0 \text{ and } \quad \varphi . \dot{\gamma} = 0. \tag{10}$$

The surface energy of the solid can be expressed based on diffusion of a crack density functional written as:

$$\Pi^s(d) = \int_\Omega \frac{\mathcal{G}_c}{2l} (d^2 + l^2 \nabla d . \nabla d) \, \mathrm{dV} \tag{11}$$

where ∇d is the spatial gradient of the phase-field variable and $\mathcal{G}_c$ and l are, respectively, the critical energy release rate and phase-field diffusive length parameter. With the above definitions, the total potential of an elastoplastic solid is expressed by:

$$\Pi = \int_\Omega g_d \left(\frac{1}{2} \boldsymbol{\varepsilon}^e : \boldsymbol{\sigma}^e + \frac{1}{2} H\alpha^2 + \sigma_y \alpha\right) \mathrm{d}\Omega + \int_\Omega \frac{\mathcal{G}_c}{2l} (d^2 + l^2 \nabla d . \nabla d) \, \mathrm{d}\Omega -$$

$$\int_\Omega \boldsymbol{b} . \boldsymbol{u} \, \mathrm{d}\Omega - \int_{\partial\Omega} \bar{\boldsymbol{t}} . \boldsymbol{u} \, d \, \partial\Omega \tag{12}$$

with $\boldsymbol{b}$ and $\bar{\boldsymbol{t}}$ being the body and traction forces, respectively, per unit volume and area of the solid. After minimization of the potential in Eq. 12 and a few arrangements, the strong form of the phase-field boundary value problem can be given by:

$$\begin{cases} \mathrm{div}(\boldsymbol{\sigma}) + \boldsymbol{b} = 0 & in \quad \Omega \\ \boldsymbol{\sigma} . \boldsymbol{N} = \bar{\boldsymbol{t}} & on \quad \partial\Omega^t \\ \boldsymbol{u} = \bar{\boldsymbol{u}} & on \quad \partial\Omega^u \end{cases} \tag{13}$$

$$\begin{cases} \frac{\mathcal{G}_c}{l}(d - l^2\Delta d) = 2(1-d)\mathcal{H} & in \ \ \Omega \\ \nabla d.n = 0 & on \ \partial\Omega \end{cases} \tag{14}$$

where the nominal stress is expressed based on the variation of the elastic energy density as:

$$\boldsymbol{\sigma} = \frac{\partial \psi^e(\boldsymbol{\varepsilon}^e, d)}{\partial \boldsymbol{\varepsilon}^e} = g_d \boldsymbol{\sigma}^e. \tag{15}$$

In the above equation, $\boldsymbol{\sigma}^e$ is the stress tensor associated with the undamaged material state. The history field parameter in Eq. (14) is defined as:

$$\mathcal{H} = \max_{[0,t]} \left(\frac{1}{2} \boldsymbol{\varepsilon}^e : \boldsymbol{\sigma}^e \right) + \langle \frac{1}{2} H \alpha^2 + \sigma_y \alpha - w_0 \rangle. \tag{16}$$

In the above function, w_0 is a scalar representing a plastic work threshold value which primarily acts as an indicator defining the instant where the updated plastic work energy should be contributed to the crack driving force evolution. The choice of w_0 influences the post-critical plastic deformation and the crack propagation as it will be discussed subsequently. The Macaulay brackets are defined as:

$$\langle x \rangle = \begin{cases} 0 & if \ \ x < 0 \\ x & if \ \ x \geq 0 \end{cases}. \tag{17}$$

4. Numerical Analysis

Finite element procedure based on staggered solution method is carried out for spatial discretization of the phase-field boundary value problem described in Eqs. 13 and 14. This procedure uses standard FE shape functions and is implemented via user coding in ABAQUS through combination of UEL and UMAT user interfaces. For detailed information regarding the ABAQUS implementation of the present phase-field model, readers are referred to [8].

The Shear Fracture specimen described in the previous section is adopted herein for the numerical analysis of fracture. The specimen geometry and dimensions are depicted Fig. 1 and a displacement-controlled boundary condition is applied to one edge of the specimen while the opposite edge is fixed. The finite element discretization is performed with fully integrated, 2D quadrilateral plane strain elements (CPE4). A refined mesh with element edge size of $b_h = 0.07$ is selected in the middle section of specimen where the fracture to be expected. The material properties corresponding to the phase-field problem are given in Table 3. Notice that the length parameter l is set to a value roughly three times larger than the minimum adopted element edge size, in accordance with the early studies, for instance in Miehe et al. [9]. Furthermore, to observe the capability of the model in the analysis of post critical material behavior, different choices of plastic threshold are utilized in the following numerical experimentation.

Table 3: Material properties used in the simulation.

$\mathcal{G}_c$ [N/mm]	l [mm]	σ_y [MPa]	w_0 [MPa]
25.0	0.2	585.06	200,800,1200

4.1. Results and Discussion

Figure 3a shows the force versus displacement curves of the experimental Shear Fracture specimens. The force corresponds to the reaction force of the machine grip. The displacement is extracted from a point close to the upper grip. The elastoplastic material responses of the three experimental samples are almost identical. In terms of failure instance, samples 1 and 3 present a similar displacement while sample 2 shows a slightly delayed fracture, which might be the result of the fact that the crack in sample 2 does not propagate instantaneously between notches, which in turn can be due to small geometrical feature and crack initiation locus differences among samples.

The significance of the fracture analysis based on the aforementioned phase-field ductile fracture model is presented in what follows. Figure 3b depicts the numerical simulation using three different plastic threshold values against the experimental curve associated with sample 1. The sensitivity analysis shows a good agreement between the numerical curve corresponds to plastic threshold value of $w_0 = 1200$ MPa with the experimental diagram, whereas the influence of w_0 can be clearly seen in defining the instant in which the displacement to failure occurs. The contour plots related to the phase-field crack evolution for $w_0 = 1200MPa$ at different deformation states are illustrated in Fig 4 (a). The cracks are expectedly initiated at the notch tips and they coalesced to form a shear band at the end of the loading process. This qualitative analysis reveals a good agreement when compared to the experimental fractured specimen shown in Fig. 4 (b).

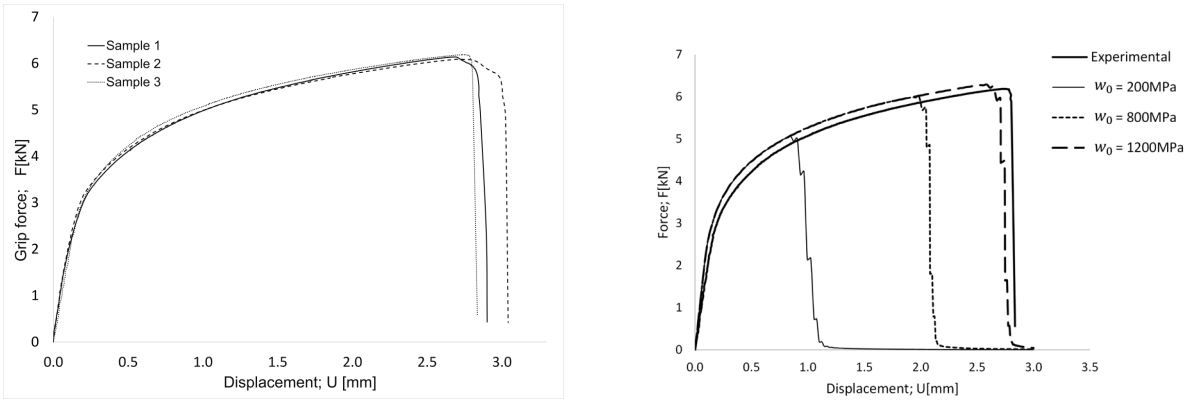

(a) (b)

Figure 3: (a) Force-displacement from experiments and (b) numerical simulations using different plastic threshold values in Shear Fracture specimen.

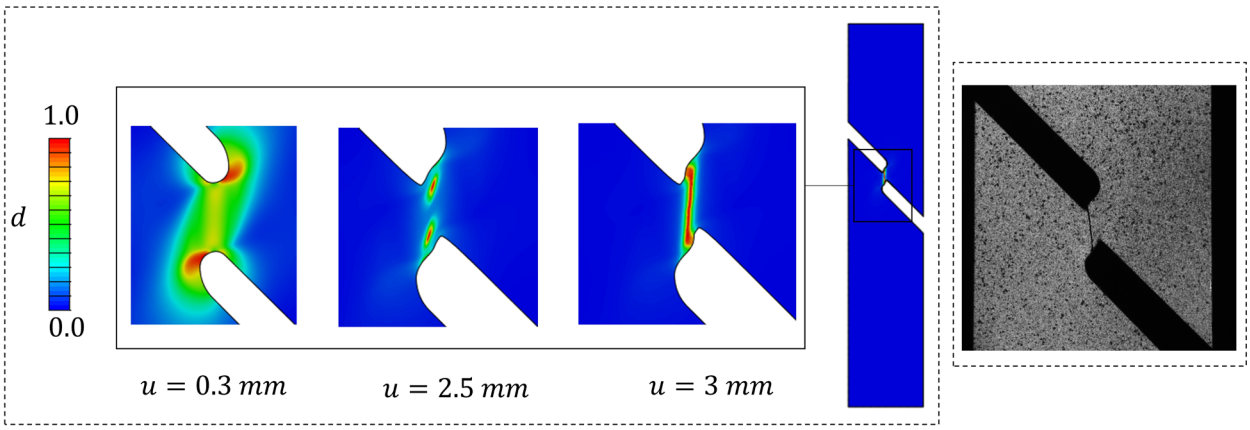

(a) (b)

Figure 4: Shear Fracture specimen (a) Phase-field crack contour at three different deformation states up until final fracture at $u = 3mm$, (b) Experimental observation of fractured specimen.

5. Conclusions

The fracture behavior of USS CR980XG3™ AHSS was analyzed in this study through a combination of experimental and numerical analyses. For this purpose, the material behavior of manufactured specimens was observed based on experimental Shear Fracture test. The numerical analysis of fracture was conducted based on phase-field model in ductile fracture. By comparing the simulated material response and the experimental measurements, a good agreement was found based on the force versus displacement diagrams. Furthermore, the evolution of damage that corresponds to the initiation and propagation of cracks was visualized throughout the loading process and compared to the experimental fractured specimen, the numerical model predictability was satisfactory. Following

these steps, future work concerns numerical experimentation on the fracture characterization on samples from this class of material, as well as specific casted parts from Duplex Stainless Steel, which entails further numerical assessments both on the level of algorithmic aspects and calibration of model parameters.

Acknowledgments

The authors gratefully acknowledge the support of General Motors and U.S. Steel for supplying the material investigated in this work. Also, it is greatly aknowledged the financial support of the Portuguese Foundation for Science and Technology (FCT) under the Project POCI-01-0145-FEDER-032466 (PTDC/EME-EME/32466/2017) – NanosFLiD – Formability of Third Generation Advanced High Strength Steels, by UE/FEDER through the program COMPETE 2020. The funding of Project NORTE-01-0145-FEDER-032419 – msCORE -Multiscale methodology with model order reduction for advanced materials and processes, cofinanced by Programa Operacional Regional do Norte (NORTE2020), through Fundo Europeu de Desenvolvimento Regional (FEDER) and by Fundação para a Ciência e Tecnologia through its component of the state budget is also acknowledged.

References

[1] B. Hance, Advanced High Strength Steel (AHSS) Performance Levels. SAE Technical Paper 2018-01-0629 (2018).

[2] B. Bourdin, G.A. Francfort, J.J. Marigo, Numerical experiments in revisited brittle fracture, J. Mech. Phys. Solids, 48 (4) (2000) 797–826.

[3] C. Miehe, S. Teichtmeister, F. Aldakheel, Phase-field modelling of ductile fracture: a variational gradient-extended plasticity-damage theory and its micromorphic regularization., Philos. Trans. A. Math. Phys. Eng. Sci., 84 (2016) 1-32.

[4] M. Ambati, T. Gerasimov, L. de Lorenzis, Phase-field modeling of ductile fracture, Comput. Mech., 55 (2015) 1017–1040.

[5] M.J. Borden, T.J.R. Hughes, C.M. Landis, A. Anvari, I.J. Lee, A phase-field formulation for fracture in ductile materials: Finite deformation balance law derivation, plastic degradation, and stress triaxiality effects, Comput. Methods Appl. Mech. Eng., 312 (2017) 130-166.

[6] C. Samaniego, J. Ulloa, P. Rodríguez, G. Houzeaux, M. Vázquez, E. Samaniego, A phase-field model for ductile fracture with shear bands: a parallel implementation, 200 (2021) 106424.

[7] R.O. Santos, L.P. Moreira, M.C. Butuc, G. Vincze, A.B. Pereira, Damage analysis of third-generation advanced high strength steel based on the Gurson-Tvergaard-Needleman (GTN) model, Metals, 12 (2022) 214.

[8] E. Azinpour, D.J. Cruz, J.M.A. Cesar de Sa, A. Santos, Phase-field approach in elastoplastic solids: application of an iterative staggered scheme and its experimental validation, Comput. Mech., 68 (2021) 255-269.

[9] C. Miehe, F. Welschinger, M. Hofacker, Thermodynamically consistent phase-field models of fracture: Variational principles and multi-field FE implementations, Int. J. Numer. Methods Eng., 83 (10) (2010) 1273–1311.

[10] Y. Lou, J.W. Yoon, Correlation of the maximum shear stress with micro-mechanisms of ductile fracture for metals with high strength to-weight ratio. Int. J. of Mechanical Sciences, 146-147 (2018) 583-601.